



# Fish-scale structured g-C<sub>3</sub>N<sub>4</sub> nanosheet with unusual spatial electron transfer property for high-efficiency photocatalytic hydrogen evolution



Bo Lin, Hua An, Xiaoqing Yan, Tianxi Zhang, Jinjia Wei, Guidong Yang\*

Department of Chemical Engineering, School of Chemical Engineering and Technology, Xi'an Jiaotong University, Xi'an 710049, China

## ARTICLE INFO

### Article history:

Received 25 January 2017

Received in revised form 15 March 2017

Accepted 25 March 2017

Available online 27 March 2017

### Keywords:

Fish-scale

g-C<sub>3</sub>N<sub>4</sub>

Nanosheet

Unusual spatial electron transfer

Photocatalytic hydrogen evolution

## ABSTRACT

Grafting the structures in nature onto g-C<sub>3</sub>N<sub>4</sub> is an interesting and fascinating protocol to highly optimize its performances. Herein, a novel opened-up fish-scale structured g-C<sub>3</sub>N<sub>4</sub> nanosheet has been synthesized via a simple one-step solvothermal method for photocatalytic hydrogen evolution. The unique fish-scale structure endows g-C<sub>3</sub>N<sub>4</sub> with unusual spatial electron transfer property, which means that the photogenerated electrons selectively migrate along the flat direction to the edges of fish-scale flakes. This property well reveals the transfer path of photogenerated charges and the origin of high charge separation efficiency in photocatalytic reaction, thus yielding a remarkable catalytic activity (a hydrogen-evolution rate of 1316.35  $\mu\text{mol h}^{-1}\text{g}^{-1}$ ), nearly 20 and 2.93 times higher than that of bulk g-C<sub>3</sub>N<sub>4</sub> and exfoliated g-C<sub>3</sub>N<sub>4</sub> nanosheet. Besides, the fish-scale structured g-C<sub>3</sub>N<sub>4</sub> also owns a superior durability and stability, indicating an outstanding potential application in solar fuel production. The research results would provide a platform for the design and construction of high-performance photocatalysts with highly-efficient charge separation.

© 2017 Published by Elsevier B.V.

## 1. Introduction

Mimicking the diverse structures in nature to design and construct nanostructures is a fascinating protocol for obtaining the productions with the desired properties. As reported, the mimic nature-like nanostructures (MNNs) greatly optimize the performances of materials. Concurrently, they could endow materials with special and novel properties, which enable them to be candidates in hydrogen evolution, CO<sub>2</sub>-to-CO conversion, emitting materials and lithium ion batteries [1–3]. For example, Wang *et al.* have reported a helical graphitic carbon nitride synthesized by using chiral SiO<sub>2</sub> as the template, and it exhibited a superior photocatalytic activity for CO<sub>2</sub> reduction and water splitting, particularly, such helical nanostructure creates a novel chirality of photocatalysis for the material [1]. In the community of MNNs, a unique fish-scale structure emerges as a shining star owing to its inimitable properties: Numerous pores are produced in the framework of the fish-scale structured materials, these pores introduce massive optical absorption active sites to efficiently capture photons and absorb sunlight [4]. Meanwhile, the multiple scattering and

reflecting effects are created by the spatial arrangement of the fish-scale flakes, these effects avail to prolong the light residence time and enhance the light harvesting efficiency [5]. Most importantly, the photogenerated electrons selectively migrate along the direction parallelly with fish-scale flat, and gather on the edges of fish-scale flakes, greatly improving photogenerated charges separation efficiency. Hence, the grafting of fish-scale structure onto the nanomaterials opens a brand new window for designing and constructing photocatalysts with highly-efficient charge separation and outstanding catalytic performance.

Recently, graphitic carbon nitride (simplified as g-C<sub>3</sub>N<sub>4</sub>) has motivated intense research in diverse applications, such as water treatment [4], hydrogen evolution [6], CO<sub>2</sub> reduction [7] and fuel cell [8] due to excellent optical and electronic properties, superior thermal and chemical stability, easily tailorable electronic structure and environmental friendliness. Nevertheless, the pristine bulk g-C<sub>3</sub>N<sub>4</sub> still suffers from multiple limitations, such as low surface area, marginal visible-light absorption and poor quantum efficiency [9]. Considerable efforts have been made to optimize the performances of g-C<sub>3</sub>N<sub>4</sub> by tailoring structure, morphology, texture, optical and electronic properties [10–12]. More recently, preparation of g-C<sub>3</sub>N<sub>4</sub> with mimic nature-like nanostructures, especially with the unique opened-up fish-scale structure, is a fairly effective way to highly optimize properties and greatly enhance activity of g-

\* Corresponding author.

E-mail address: [guidongyang@xjtu.edu.cn](mailto:guidongyang@xjtu.edu.cn) (G. Yang).

C<sub>3</sub>N<sub>4</sub>. By contrast with traditional bulk g-C<sub>3</sub>N<sub>4</sub> and even exfoliated g-C<sub>3</sub>N<sub>4</sub> nanosheet, the fish-scale structured g-C<sub>3</sub>N<sub>4</sub> nanosheet has the inimitable structural advantages, including greatly enhanced sunlight utilization, high active surface area and porosity, highly-efficient charge separation and transfer. Therefore, synthesis of opened-up fish-scale structured g-C<sub>3</sub>N<sub>4</sub> nanosheet is a promising approach to significantly enhance the photocatalytic activity of g-C<sub>3</sub>N<sub>4</sub>. However, thus far, there is no report available on the construction of opened-up fish-scale structured g-C<sub>3</sub>N<sub>4</sub> with a prominent photocatalytic performance.

Herein, we for the first time report the construction of a novel opened-up fish-scale structured g-C<sub>3</sub>N<sub>4</sub> nanosheet (simplified as FSGNs) via a simple one-step solvothermal method. The FSGNs samples exhibited a superior hydrogen evolution activity and outstanding stability relative to bulk g-C<sub>3</sub>N<sub>4</sub> (BCN) and pristine g-C<sub>3</sub>N<sub>4</sub> nanosheet (CNNs). The three scientific issues, including visible-light absorption efficiency, active surface area and porosity, photogenerated charges separation and transfer, were investigated to explore the intrinsic link between the structure-induced unusual spatial electron transfer property and greatly enhanced photocatalytic activity for FSGNs.

## 2. Experimental

### 2.1. Material synthesis

All reagents for synthesis and analysis were commercially available and used without further treatment.

#### 2.1.1. Synthesis of bulk g-C<sub>3</sub>N<sub>4</sub>

3 g of melamine was directly calcined at 550 °C for 4 h in a tube furnace with a heating ramp of 2.3 °C min<sup>-1</sup> in nitrogen atmosphere, the resultant powder was collected for the further use.

#### 2.1.2. Synthesis of pristine g-C<sub>3</sub>N<sub>4</sub> nanosheet

2 g of bulk g-C<sub>3</sub>N<sub>4</sub> was exposed to air and calcined at 520 °C for 4 h, the final powder was collected for using as a reference.

#### 2.1.3. Synthesis of fish-scale structured g-C<sub>3</sub>N<sub>4</sub> nanosheet

0.2 g of above g-C<sub>3</sub>N<sub>4</sub> nanosheet was dispersed in 30 mL of ethanediol and vigorously stirred for 0.5 h at room temperature. Then a mixture of certain amount of polyvinylpyrrolidone (PVP) K30 (M<sub>w</sub> ~ 40 000) and hexadecyl trimethyl ammonium Bromide (CTAB) was added in the above dispersion solution, underwent the ultrasound treatment for 0.5 h and vigorously stirred at same temperature for 0.5 h. Finally, the above mixture solution was transferred to a 100 mL Teflon-lined stainless steel autoclave and heated at a series of different temperatures for 6 h. After cooling down to room temperature, collect the sample by the centrifugation and rinse several times with deionized water and ethanol to remove the PVP and CTAB, and then dry in a drying oven at 80 °C for 12 h. The obtained samples with different treatment temperatures of 40 °C, 80 °C and 120 °C were denoted as FSGNs1, FSGNs2 and FSGNs3, respectively.

### 2.2. Characterization

The microstructures and morphologies of the obtained samples were observed with a field-emission scanning electron microscope (JEOL, JSM-6700F). The geometry and surface states of all samples were further investigated by a transmission electron microscopy (JEOL, JEM-2100). The elementary composition was analyzed by the affiliated energy dispersive X-ray spectroscopy (EDX) instruments belonged to the above SEM and TEM, respectively. The crystal structure of products was carried out using a powder X-ray diffraction (SHIMADZU, Lab X XRD-6100). UV–vis

diffuse reflectance spectra (DRS) were recorded with a UV–vis spectrophotometer (SHIMADZU, UV-2600). The BET surface areas were collected on an automatic BET analyzer (Auantachrome, Autosorb-iQ-TPX), and the samples were degassed at 160 °C for 6 h prior to the nitrogen adsorption measurements. The photoluminescence (PL) emission spectra were tested using a fluorescence spectrophotometer (HORIBA, JY Fluorolog-3) with 340 nm excitation wavelength. The time-resolved fluorescence emission spectra were performed on a PTI QM-400 luminescence spectrometer with 400 nm as the excitation wavelength.

### 2.3. Photocatalytic activity measurement

Photocatalytic hydrogen evolution was carried out in an outer Pyrex reactor (100 mL). For each reaction, 0.05 g of sample was added to 50 mL of aqueous solution containing 10 vol.% of tri-ethanolamine (sacrificial electron donor). 3 wt% of Pt was in-suit photodeposited onto the surface of photocatalysts using H<sub>2</sub>PtCl<sub>6</sub> as the Pt-cocatalyst precursor. The reaction solution was bubbled with high purity nitrogen for 0.5 h to remove air completely prior to irradiation. Then the photocatalytic reaction was launched by using a 300 W Xenon lamp (HSX-F300, Beijing NBET) equipped with a 420 nm UV filter (HSX-UV300). The generated gases were determined by a SP-2100A type gas chromatograph (Beifen-Ruili, equipping with 5 Å molecular sieve and a TCD detector).

Additionally, 10 wt% of Pt was in-suit photodeposited onto the surface of FSGNs2 for 2 h under the same conditions to explore the photodeposited positions of Pt particles.

### 2.4. Photoelectrochemical measurement

The photocurrent response of all products was recorded at an electrochemical station (CHI 660D, Chenhua, China) using a three-electrode system. The electrolyte was Na<sub>2</sub>SO<sub>4</sub> aqueous solution (2 M). A platinum wire was used as the counter electrode of system, and Ag/AgCl electrode was selected as the reference electrode. The glassy carbon electrodes containing obtained samples were acted as the working electrodes.

## 3. Results and discussion

The overall approach for the formation of FSGNs is schematically illustrated in Fig. 1. The g-C<sub>3</sub>N<sub>4</sub> nanosheet (CNNs) is obtained via thermal oxidation exfoliation of initial bulk g-C<sub>3</sub>N<sub>4</sub> (BCN) annealing at 520 °C for 4 h in air, due to the destruction of hydrogen bonds among g-C<sub>3</sub>N<sub>4</sub> layers [13]. Then PVP and CTAB molecules as the porogenic agents are readily absorbed on plentiful active sites of CNNs surface, and occupy much surrounding space of CNNs. After that, when the CNNs with absorbed PVP and CTAB molecules is heated under the solvothermal condition, CTAB molecules can generate a large number of bubbles, which thus prompt the CNNs to deform and form massive pores. Besides, the above PVP and CTAB molecules can be covered by the distorted CNNs and occupy its inside space. After removing the residual porogen molecules, the numerous cavities are thus created in the original space occupied by PVP and CTAB molecules [14–16]. Ultimately, the unique and well-defined FSGNs with a fish-scale flake width of about 120 nm is obtained in this way.

Fig. 2a–e shows the scanning electron microscopy (SEM) images of the obtained products. As shown in Fig. 2a, a typical aggregated bulk structure related to BCN can be observed. In Fig. 2b, a micron-sized flat nanosheet composed with massive particles (CNNs) can be easily found as a result of thermal oxidation exfoliation. After the solvothermal treatment at 40 °C for 6 h, the resultant FSGNs1 sample exhibits a partially wrinkled porous structure similarly to the curved fish scales, while other part of FSGNs1 still maintains

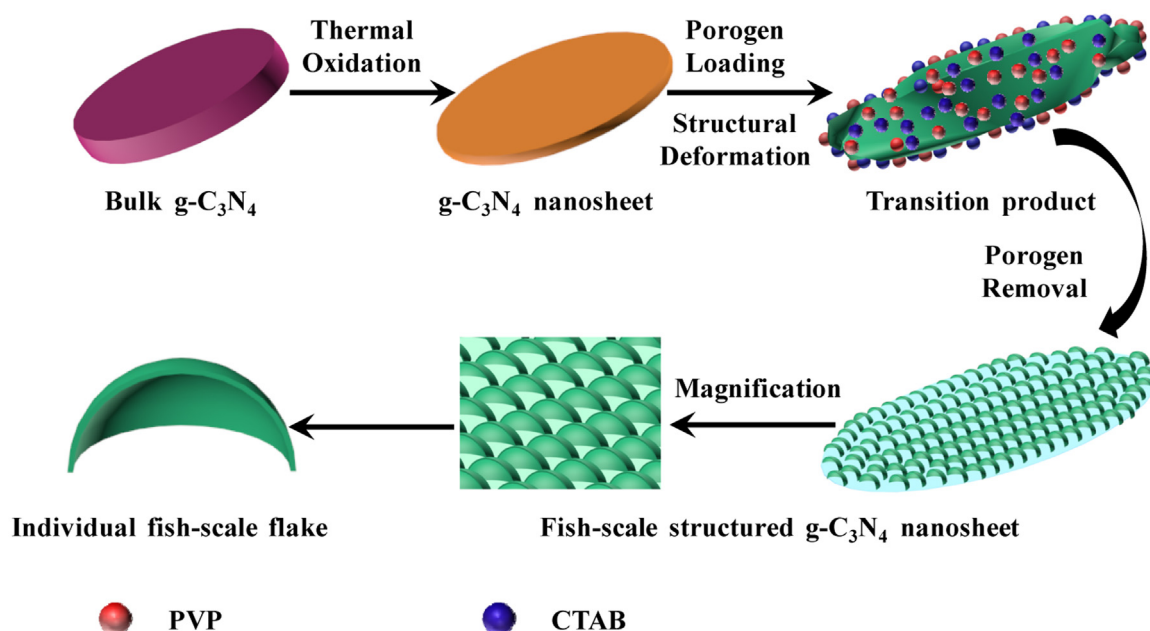


Fig. 1. Schematic illustration of formation process of fish-scale structured  $\text{g-C}_3\text{N}_4$  nanosheet.

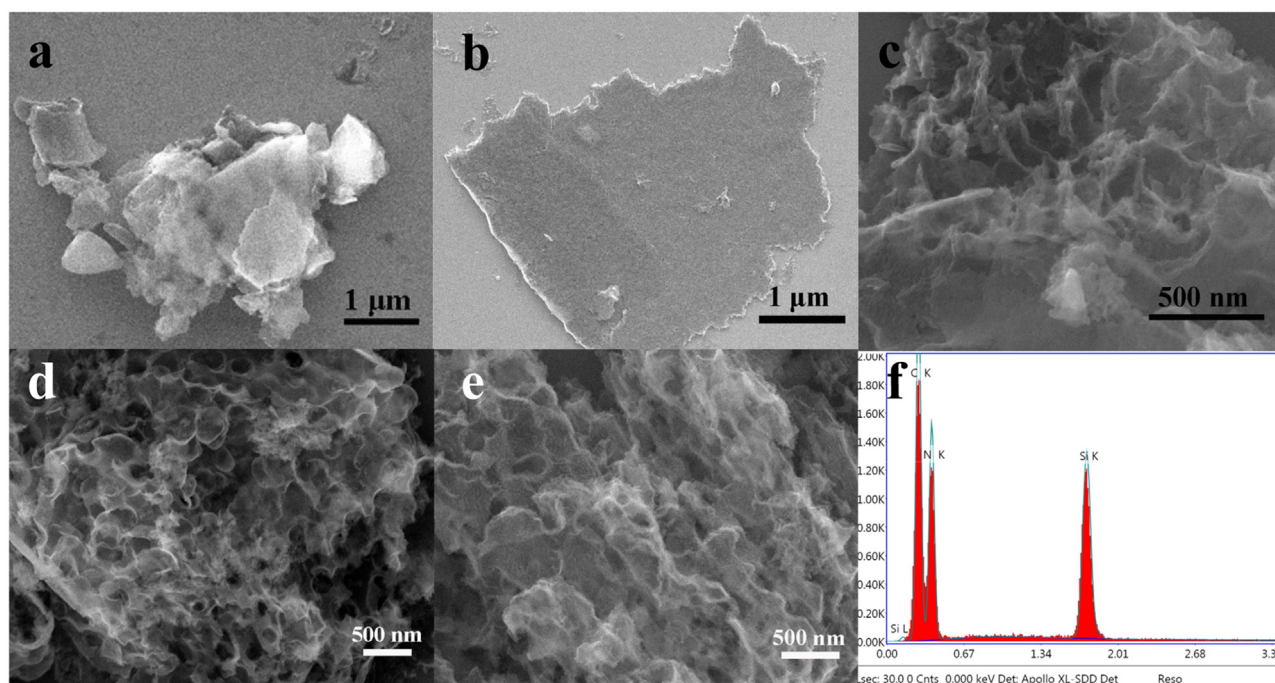


Fig. 2. SEM images of (a) BCN, (b) CNNs, (c) FSGNs1, (d) FSGNs2 and (e) FSGNs3. EDX image (f) of FSGNs2. The strong signal peak of Si is derived from the silicon substrate with the uniformly loaded sample in the SEM test.

the nanosheet architecture (Fig. 2c). When the treatment temperature reaches  $80^\circ\text{C}$ , a large-area uniform fish-scale structure with massive macropores is displayed in the SEM image of FSGNs2 (Fig. 2d). However, compared with FSGNs2, the FSGNs3 (treating at  $120^\circ\text{C}$ ) shows a relatively irregular fish-scale microstructure, and lots of fish-scale flakes are destroyed (Fig. 2e). The above observations indicate that the CNNs sample starts to deform and curl with the increase of solvothermal temperature, and gradually forms the unique opened-up fish-scale structured nanosheet with the help of the porogens. Besides, it thoroughly transforms into the regular and well-defined fish-scale structure at  $80^\circ\text{C}$ , then the excessive tem-

perature contributes to the collapse and destruction of fish-scale flakes. Fig. 2f shows the energy-dispersive X-ray analysis (EDX) of FSGNs2, which further demonstrates the formation of  $\text{g-C}_3\text{N}_4$  material.

The transmission electron microscopy (TEM) images give further insight into the morphologies of the above samples. Fig. 3a shows the micron-sized bulk morphology of BCN, while Fig. 3b shows the CNNs sample with a smooth thinner nanosheet morphology. It can be clearly seen from Fig. 3c (FSGNs1), the fish-scale structured flakes appear in the interior of the large-area flat  $\text{g-C}_3\text{N}_4$  nanosheet. In the typical TEM images of FSGNs2 (Fig. 3d), a



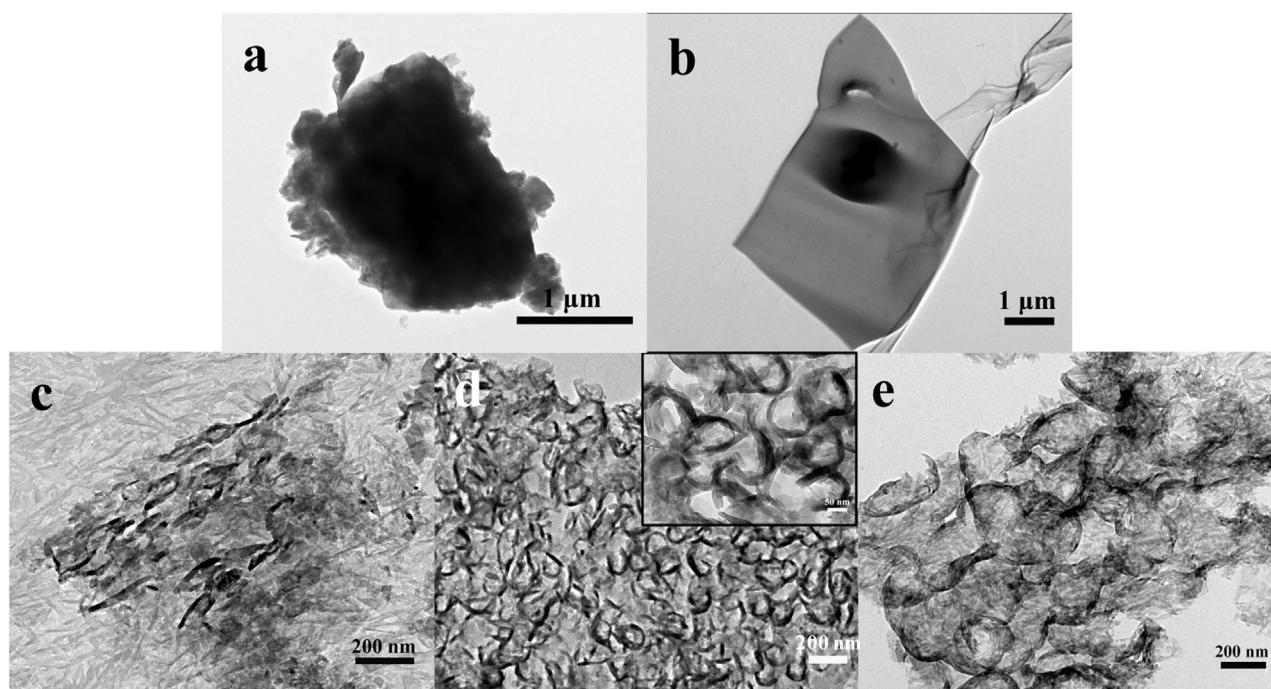


**Fig. 3.** TEM images of (a) BCN, (b) CNNs, (c) FSGNs1, (d) FSGNs2 and (e) FSGNs3. Inset in (d): The local magnification TEM of FSGNs2.

large scale of fish-scale flakes interconnect together and constitute an opened-up micron-sized nanosheet. To better observe the morphology of the fish-scale flakes, the local magnification TEM of FSGNs2 is shown in inset of Fig. 3d, where uniform fish-scale  $g\text{-C}_3\text{N}_4$  flakes with an average width of about 120 nm are found accompanied with abundant micropores, mesopores and macropores. The unique opened-up fish-scale structured nanosheet effectively facilitates the photogenerated charge separation and transfer by accelerating the photogenerated electrons to selectively transfer to the edge of fish-scale flakes. Fig. 3e shows a cracked and irregular  $g\text{-C}_3\text{N}_4$  nanosheet with the outline of residual fish-scale flakes, manifesting a seriously textural deformation of FSGNs, as evidenced by SEM observations in Fig. 2e.

Fig. 4a displays the typical X-ray diffraction patterns (XRD) of the synthesized photocatalysts. In all XRD profiles, a weak peak at  $13.0^\circ$  can be easily found belonging to the (100) crystal plane, which is due to the in-plane repetitive tri-s-triazine units [17,18]. With respect to BCN, a sharp and strong peak at  $27.4^\circ$  appeared in the curve is corresponded to the (002) interlayer reflection of periodic melon networks with a  $d$ -spacing value of 0.325 nm [19–21]. However, the (002) reflection peaks of CNNs and three FSGNs samples show a shift from  $27.4^\circ$  to  $27.8^\circ$  (a corresponding  $d$ -spacing value of 0.321 nm), indicating that the average interplane distance of these nanosheet samples has declined 0.04 nm compared with that of BCN [22]. This is because that the potentially undulated layers in bulk  $g\text{-C}_3\text{N}_4$  could be planarized with the temperature rising in the thermal oxidation exfoliation process, which may result in a compressed packing of single  $g\text{-C}_3\text{N}_4$  layers, thus shortening the interplane distance of the nanosheet samples [13,23,24]. It should be pointed out that the (002) reflection peak of FSGNs2 is more sharp than that of CNNs, FSGNs1 and FSGNs3, indicating that the unique and regular fish-scale structure is favorable for the improvement of crystallinity, which benefits the charge conduction and transfer from the crystal region to the reactive interface.

To shed light on the optical performances of the as-obtained products, the UV–vis diffuse reflectance spectra (DRS) of them are investigated, and the corresponding band gaps of them are estimated simultaneously. As shown in Fig. 4b, a photoabsorption

**Table 1**

The estimated values of band gap energy, valence band potential and conduction band potential for BCN, CNNs, FSGNs1, FSGNs2 and FSGNs3.

Samples	Band gap energy (eV)	Valence band potential (eV)	Conduction band potential (eV)
BCN	2.70	1.58	−1.12
CNNs	2.93	1.70	−1.23
FSGNs1	2.86	1.66	−1.20
FSGNs2	2.77	1.62	−1.15
FSGNs3	2.89	1.68	−1.21

edge at up to 460 nm can be easily discovered in the profile of BCN, which corresponds to its estimated values of band gap ( $E_g$ ), valence band potential ( $E_{VB}$ ) and conduction band potential ( $E_{CB}$ ) for 2.7 eV, 1.58 eV and −1.12 eV, respectively (Fig. 4c and Table 1), suggestive of a routine visible-light responsive ability, as evidenced by the previous report [25]. However, a clear hypsochromic shift from 460 nm to 423 nm is observed for CNNs, this is because the exfoliated  $g\text{-C}_3\text{N}_4$  layers closely stack and interact in the thermal oxidation treatment process, which produces an evident quantum confinement effect, thus making the valence band edge and conduction band edge shift away from each other, thus generating an enlarged band gap [6,13,17,23,26,27]. Excitingly, the FSGNs series samples show obviously reduced band gaps in comparison with CNNs (Fig. 4c and Table 1), especially for the FSGNs2 sample, which shows a narrowed band gap of 2.77 eV, low  $E_{VB}$  of 1.62 eV and high  $E_{CB}$  of −1.15 eV, respectively. This phenomenon can be attributed to the facts that FSGNs2 owns the more regular and intact opened-up fish-scale structure relative to FSGNs1 and FSGNs3, and the two former samples retain the partial or residual flat sheet-like structure (see SEM and TEM images), these facilitate FSGNs2 to suffer from the less limitation derived from quantum confinement effect than the other two samples, thus leading to the narrower band gap. Additionally, in comparison to BCN and CNNs, the visible-light harvesting ability of the three FSGNs samples has been remarkably improved. Meanwhile, FSGNs1 and FSGNs2 have much more powerful optical absorption ability compared with FSGNs3. These are

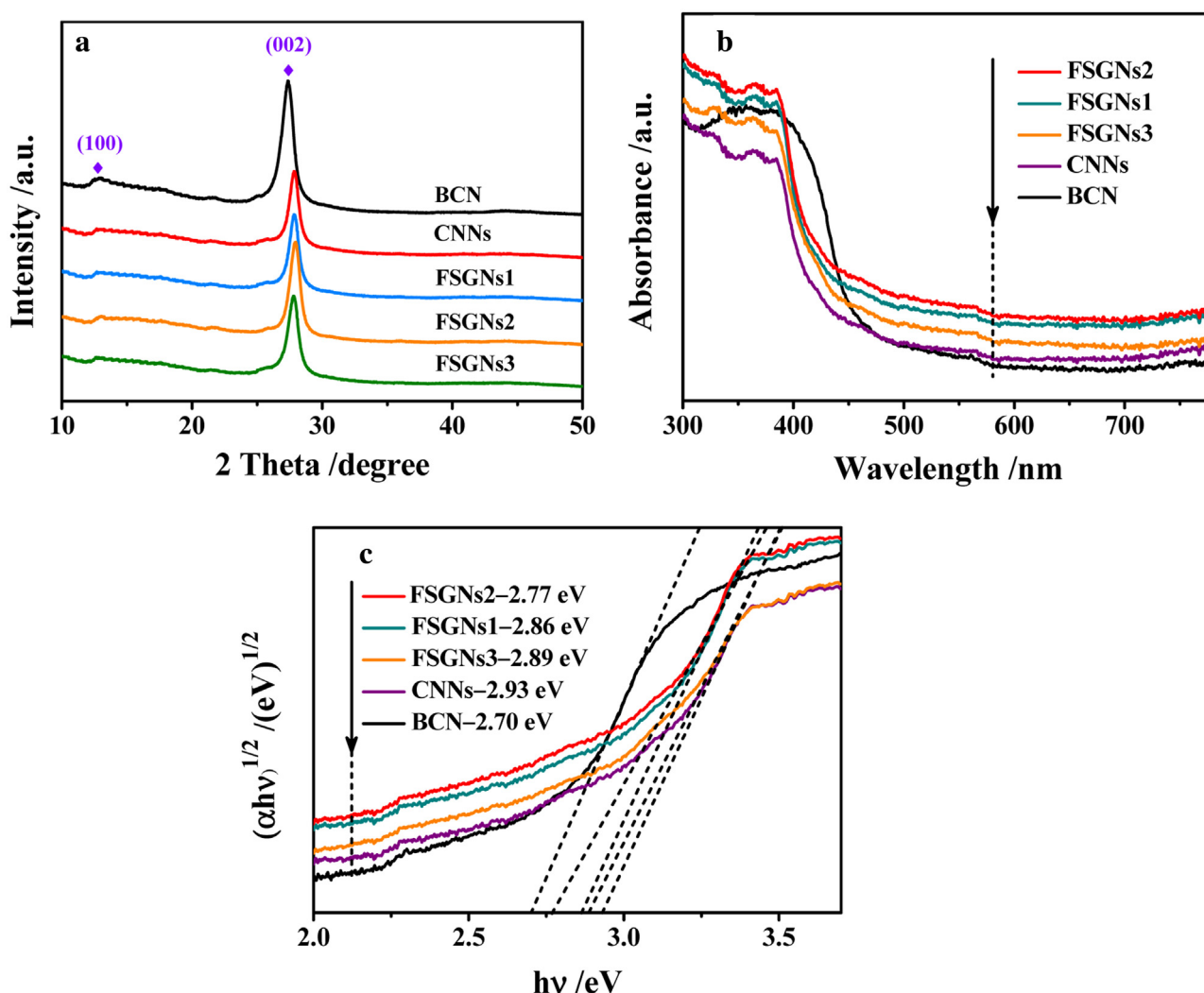


**Fig. 4.** X-ray diffraction patterns (a) of BCN, CNNs, FSGNs1, FSGNs2 and FSGNs3. UV-vis diffuse reflectance spectra (b) and plots of  $(\alpha h\nu)^{1/2}$  versus energy ( $h\nu$ ) (c) for BCN, CNNs, FSGNs1, FSGNs2 and FSGNs3.

due to the synthetic effects of multiple reflections and scatterings produced by the unique spatial distribution of the fish-scale flakes, abundant exposed defect sites derived from numerous introduced micropores, mesopores and macropores as well as massive exposed edge surfaces of fish-scale flakes [6,17].

Fig. 5a shows the  $N_2$  adsorption-desorption isotherms of the as-prepared products. A typical IV isotherm with a type H3 hysteresis loop in 0.7–1.0 relative pressure ( $p/p_0$ ) could be observed in all isotherm profiles, suggestive of the presence of mesopores and macropores, as evidenced by the observations of SEM in Fig. 2 and TEM in Fig. 3 [28,29]. By contrast, the nitrogen adsorption/desorption amounts of the three FSGNs samples have significantly increased than that of BCN and CNNs, especially FSGNs2, indicating the introduction of numerous pores with the construction of the unique opened-up fish-scale structure [30]. The pore-size distributions estimated by the BJH and MP methods over different samples are illustrated in Fig. 5b and Fig. 5c, respectively. As shown in Fig. 5b, a similar pore-size (radius) distribution in the region of 1.5–9 nm is presented in all photocatalysts, and a gradually increased peak at approximately 2 nm can be clearly observed from BCN to CNNs then to the FSGNs samples, manifesting more micropores and mesopores endowed by the fish-scale structure [30]. The formation of micropores is also proved by the MP pore-size (diameter) distribution profiles that a gradually increased peak

**Table 2**  
Textural properties for BCN, CNNs, FSGNs1, FSGNs2 and FSGNs3.

Samples	$S_{BET}$ ( $m^2 g^{-1}$ )	Average pore size (nm)	Pore volume ( $cm^3 g^{-1}$ )
BCN	10.71	35.79	0.0959
CNNs	100.46	24.63	0.4009
FSGNs1	132.39	17.08	0.6613
FSGNs2	210.33	15.62	1.2951
FSGNs3	130.29	18.07	0.5565

at about 0.7 nm has been found (Fig. 5c). It is noted that the created micropores with the diameter of about 0.7 nm is favorable for the selective diffusion, absorption and photocatalytic reaction for  $H_2O$  molecules (a approximate diameter of 0.324 nm) as well as the accommodation of photogenerated charges [31].

Textural properties for BCN, CNNs, FSGNs1, FSGNs2 and FSGNs3 are summarized in Table 2. As shown in Table 2, in comparison to BCN (35.79 nm) and CNNs (24.63 nm), the average pore sizes of the FSGNs samples (17.08 nm, 15.62 nm and 18.07 nm for FSGNs1, FSGNs2 and FSGNs3, respectively) have significantly reduced, suggestive of the generation of massive micropores and mesopores, keeping with the results of the pore-size distributions in Fig. 5b and Fig. 5c. The values of BET surface area and pore volume of the FSGNs samples ( $132.39 m^2 g^{-1}$  and

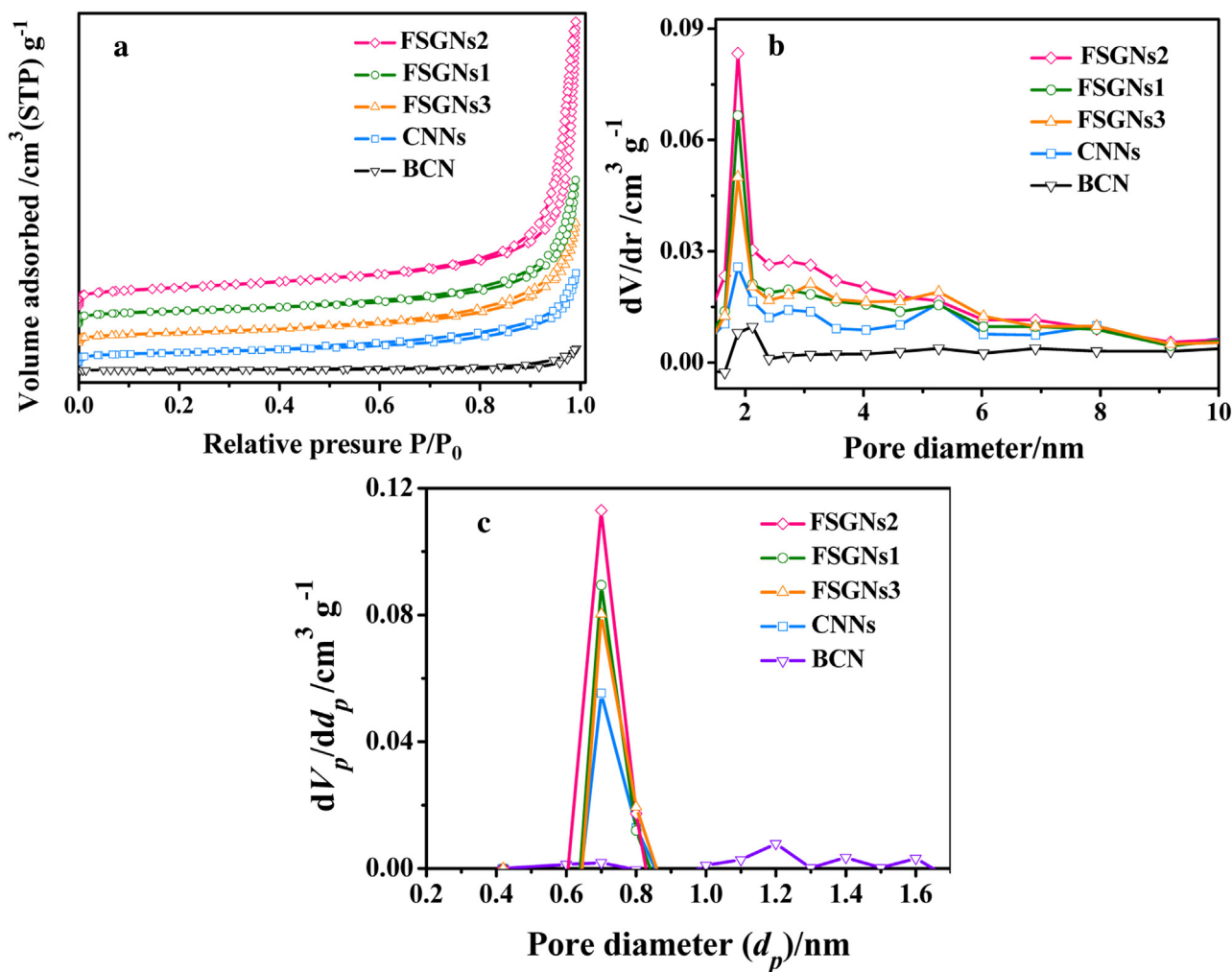


**Fig. 5.** (a) Nitrogen adsorption-desorption isotherms for BCN, CNNs, FSGNs1, FSGNs2 and FSGNs3. (b) Pore-size (radius) distributions using the BJH method and (c) pore-size (diameter) distributions using the MP method for BCN, CNNs, FSGNs1, FSGNs2 and FSGNs3.

0.6613 cm<sup>3</sup> g<sup>-1</sup> for FSGNs1, 210.33 m<sup>2</sup> g<sup>-1</sup> and 1.2951 cm<sup>3</sup> g<sup>-1</sup> for FSGNs2, 130.29 m<sup>2</sup> g<sup>-1</sup> and 0.5565 cm<sup>3</sup> g<sup>-1</sup> for FSGNs3) are much higher than BCN (10.71 m<sup>2</sup> g<sup>-1</sup> and 0.0959 cm<sup>3</sup> g<sup>-1</sup>) and CNNs (100.46 m<sup>2</sup> g<sup>-1</sup> and 0.4009 cm<sup>3</sup> g<sup>-1</sup>), this indicates that construction of unique opened-up fish-scale structure favors the significant enhancement of surface area and pore volume, thus benefiting the mass transfer, adsorption and photocatalytic reaction of reactant molecules. Furthermore, FSGNs2 displays the highest BET surface area and pore volume relative to FSGNs1 and FSGNs3, further demonstrating that the more uniform and intact fish-scale structure contributes to the optimal textural properties.

The photoluminescence (PL) spectra of various samples are detected to investigate the photoinduced charge carrier behaviors of trapping, migration and recombination. As can be seen in Fig. 6a, the initial bulk g-C<sub>3</sub>N<sub>4</sub> (BCN) shows an intense and broad emission peak at around 460 nm, indicative of a band gap of 2.7 eV, as confirmed by DRS results in Fig. 4b and c. Besides, its fairly high intensity indicates a considerably high charge recombination rate caused by its intrinsic geometry structure [32]. The prominent blue-shifts appear in curves of CNNs and FSGNs series samples due to their widening bandgaps [19], as described in DRS analysis in Fig. 4b and c. Concurrently, the fluorescence is partially quenched occurred in profiles of these samples, especially in the spectrum of FSGNs2 that shows an extremely low fluorescence intensity, indicating that the opened-up fish-scale architecture could effectively

**Table 3**

The radiative fluorescence lifetimes and relative percentages of photoinduced charge carriers in CNNs and FSGNs2.

Samples	$\tau_1$ (ns) (Rel.%)	$\tau_2$ (ns) (Rel.%)
CNNs	1.30 (37.85)	6.64 (62.15)
FSGNs2	2.63 (29.52)	9.61 (70.48)

enhance the separation and transfer of photogenerated charges, which is realized by defect introduction for blocking the recombination of charges as well as selective electron migration from the bulk to the fish-scale flake edges [33,34]. This analysis is further proved by transient photocurrent responses (Fig. 6b), which shows the structural benefits of intact opened-up fish-scale structure in photocurrent generation relative to BCN, CNNs, partial and damaged FSGNs samples, suggesting an expected outstanding catalytic activity in photocatalytic H<sub>2</sub> evolution. To better understand the fish-scale structure-induced effects on the behaviors of photogenerated charges, the time-resolved fluorescence decay spectra of CNNs and FSGNs2 have been measured. As shown in Fig. 6c, the fluorescent intensities of both photocatalysts exhibit an exponential decay, and FSGNs2 displays a slower decay kinetics than CNNs. After fitting the above decay spectra, two radiative lifetimes with different corresponding percentages are given in Table 3. Both short lifetime ( $\tau_1$ ) and long lifetime ( $\tau_2$ ) for charge carriers show a clearly increased form CNNs ( $\tau_1 = 1.30$  ns,  $\tau_2 = 6.64$  ns) to FSGNs2 ( $\tau_1$



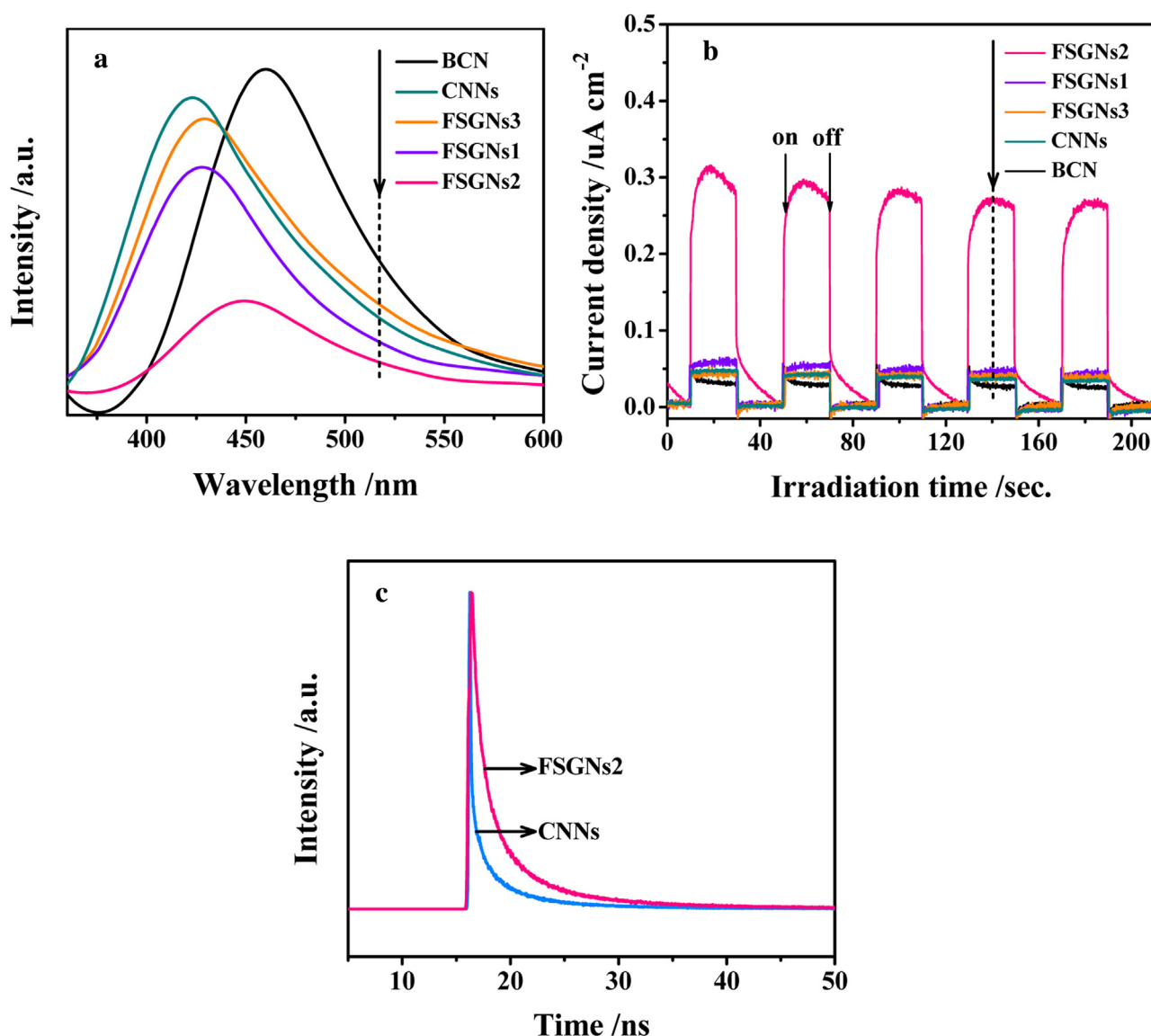


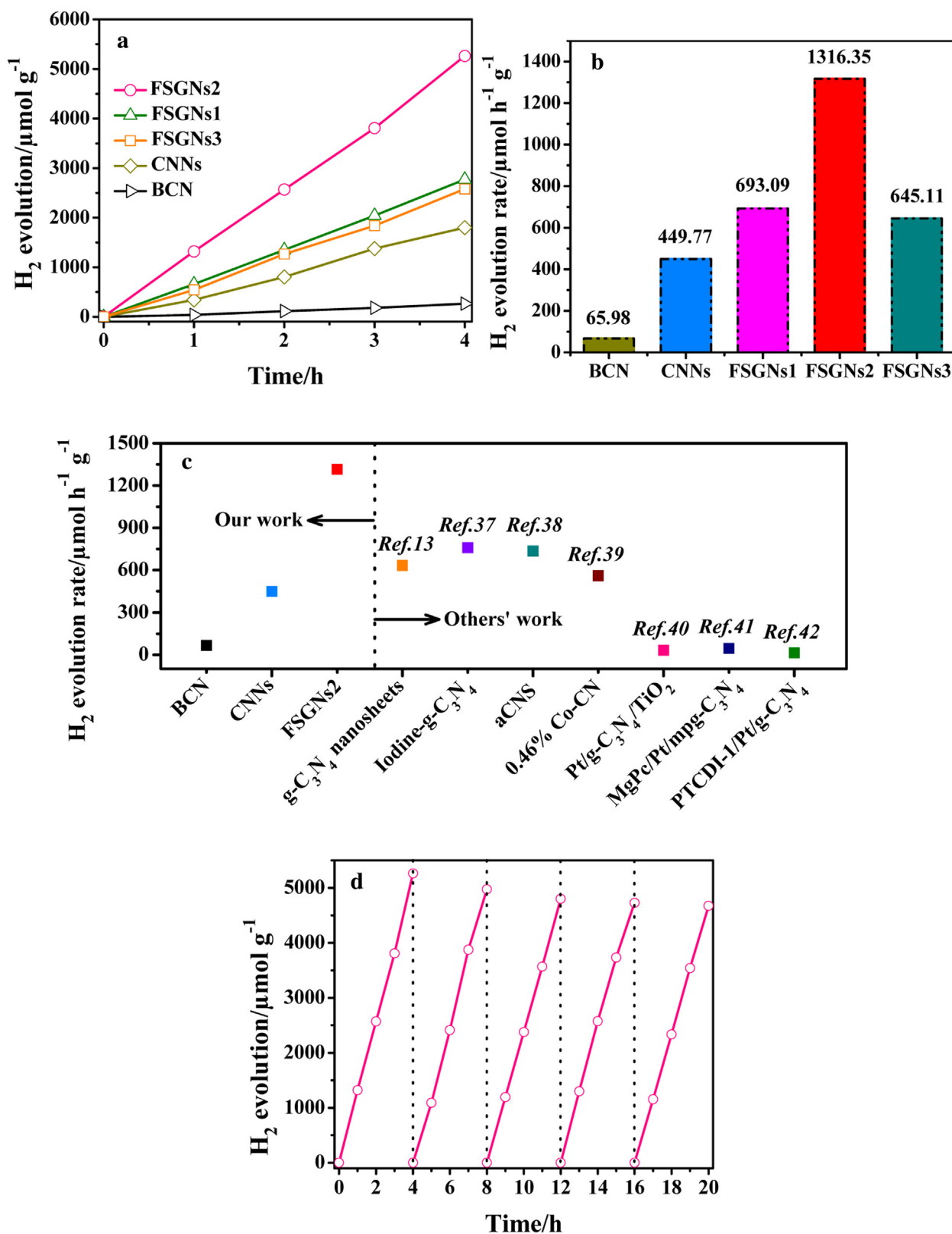
**Fig. 6.** (a) Photoluminescence (PL) spectra and (b) transient photocurrent responses for BCN, CNNs, FSGNs1, FSGNs2 and FSGNs3. (c) Time-resolved fluorescence decay spectra of CNNs and FSGNs2.

= 2.63 ns,  $\tau_2$  = 9.61 ns). These indicate that the structure-induced selective electron migration property significantly facilitates the separation and migration of photogenerated charges, resulting in a greatly prolonged radiative lifetime for charge carriers. The increased radiative lifetime promotes more charges to participate in the photocatalytic reaction and thus effectively enhances the photocatalytic performance for opened-up fish-scale structured g-C<sub>3</sub>N<sub>4</sub> [35,36], conforming to the above analysis in Fig. 6a and b.

Time courses of photoinduced hydrogen evolution for different samples have been performed in the aqueous solution containing triethanolamine, employing 3 wt% of Pt in-situ photodeposited onto the surface of samples as the cocatalyst under visible light irradiation ( $\lambda \geq 420$  nm). As illustrated in Fig. 7a, all samples show a linearly increased hydrogen evolution amount remarkably consistent over time, manifesting the overall stability of samples in photoreaction. In Fig. 7b, BCN shows a poor photocatalytic activity with a low hydrogen-evolution rate (HER) of 65.98  $\mu\text{mol h}^{-1} \text{g}^{-1}$ , while CNNs displays a superior HER (449.77  $\mu\text{mol h}^{-1} \text{g}^{-1}$ ) after the thermal oxidation, which is attributed to structural advantages of g-C<sub>3</sub>N<sub>4</sub> nanosheet. Incredibly, in spite of the only formation of partial unique fish-scale structure, the HER of FSGNs1 (693.09  $\mu$

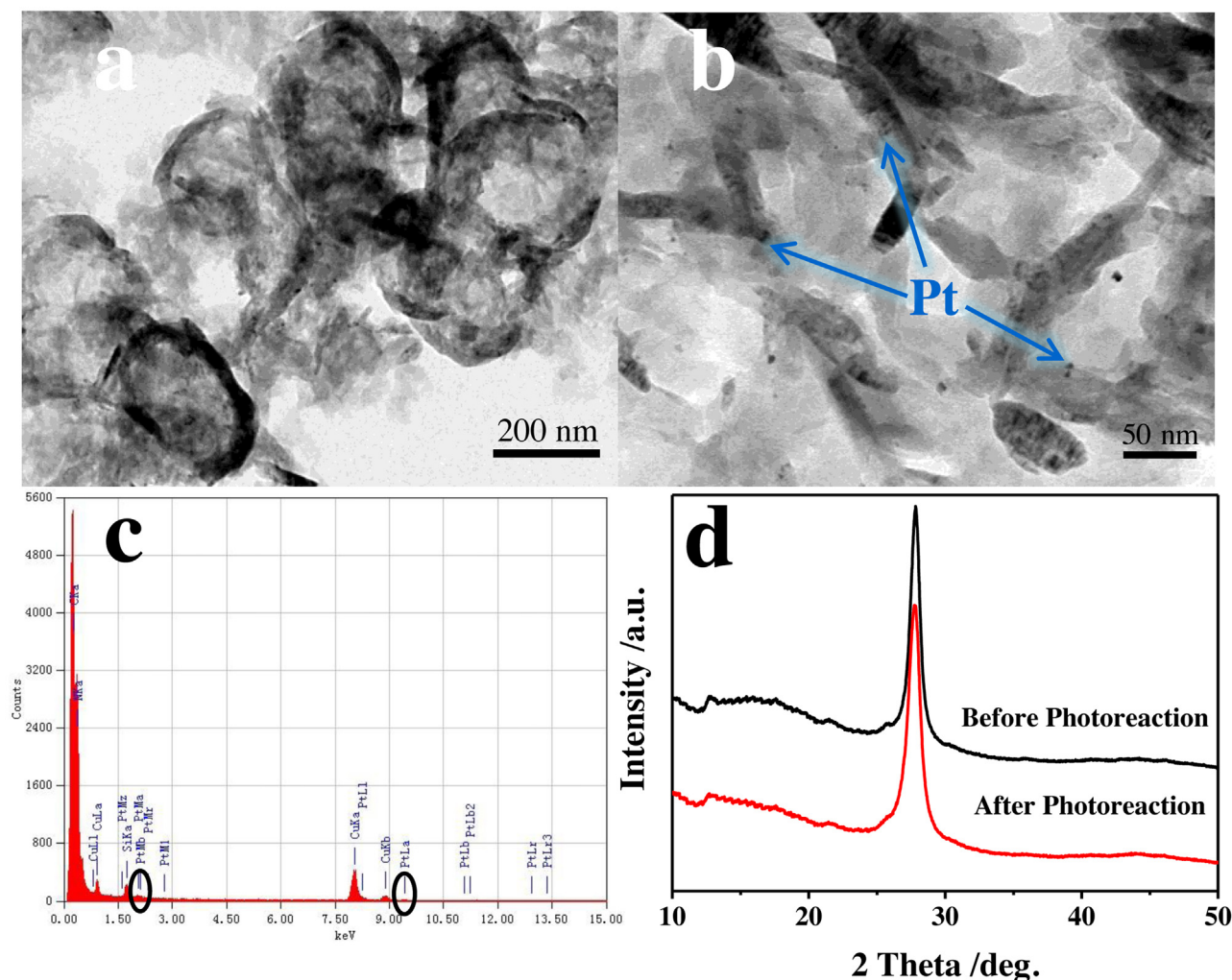
$\text{mol h}^{-1} \text{g}^{-1}$ ) is greatly improved, nearly 1.54 times than that of CNNs, strongly supporting the attractive structure-induced properties of FSGNs. As expected, the well-defined and intact opened-up fish-scale structured sample (FSGNs2) shows a remarkable hydrogen evolution performance with a HER of 1316.35  $\mu\text{mol h}^{-1} \text{g}^{-1}$ , this value is nearly 20 and 2.93 times higher than that of BCN and CNNs, even far exceeds that of FSGNs1 (693.09  $\mu\text{mol h}^{-1} \text{g}^{-1}$ ). Notably, the HER of FSGNs2 far exceeds that of most other modified g-C<sub>3</sub>N<sub>4</sub> under the same test conditions in previous reports [13,37–42] (Fig. 7c), strongly evidencing the high photocatalytic activity induced by the opened-up fish-scale structure. FSGNs3 reveals a significantly reduced HER of 645.11  $\mu\text{mol h}^{-1} \text{g}^{-1}$  in comparison to FSGNs2, which is due to the seriously structural deformation of FSGNs, further suggesting the importance of well-developed FSGNs for hydrogen evolution activity.

Fig. 7d shows the cyclic stability performance for the photocatalytic H<sub>2</sub> production over 3 wt% Pt-deposited FSGNs2 under the same conditions. The fish-scale structured sample still remains a high H<sub>2</sub> evolution activity (1168.60  $\mu\text{mol h}^{-1} \text{g}^{-1}$ , nearly 88.8% of initial HER) after five photoreactions. The TEM images of 3 wt% Pt-



**Fig. 7.** (a) Time-dependent photocatalytic hydrogen evolution and (b) hydrogen-evolution rate over different 3 wt% Pt-deposited samples under visible light irradiation ( $\lambda \geq 420$  nm). (c) Hydrogen-evolution rate over Pt-deposited BCN, CNNs and FSGNs2 in comparison with other modified Pt-deposited  $\text{g-C}_3\text{N}_4$  in previous reports under visible light irradiation. All products in (c) select triethanolamine as sacrificial electron donor. (d) Cyclic stability tests for the photocatalytic  $\text{H}_2$  production over 3 wt% Pt-deposited FSGNs2 under visible light irradiation ( $\lambda \geq 420$  nm).





**Fig. 8.** TEM images of (a,b) 3 wt% Pt-deposited FSGNs2 after cyclic stability tests. EDX image (c) of 3 wt% Pt-deposited FSGNs2 after cyclic stability tests. The signal peaks of Cu and Si are due to the carbon-supported copper net used to uniformly load samples in the TEM test. X-ray diffraction patterns (d) of FSGNs2 before and after five photoreactions.

deposited FSGNs2 after the recycled tests (Fig. 8a and b) show a relatively intact opened-up fish-scale morphology with numerous Pt nanoparticles decorated on the surface edges of fish-scale flakes, which is evidenced by the EDX image of the recycled FSGNs2 sample (Fig. 8c). Furthermore, no significant difference can be observed in the two FSGNs2 samples before and after five photoreactions in the XRD patterns (Fig. 8d). These results confirm that the opened-up fish-scale structured g-C<sub>3</sub>N<sub>4</sub> has an excellent durability and stability, indicating an outstanding potential in sustainable energy conversion.

To investigate the electron migration path on the flat of fish-scale flakes, we elaborated the photodeposited experiments of Pt nanoparticles with different amounts on the surface of FSGNs2, because Pt nanoparticles are considered as the active sites and coupled with electrons to reduce H<sub>2</sub>O molecules to produce hydrogen in photocatalytic hydrogen evolution [43–45]. In the TEM images of 3 wt% Pt-deposited FSGNs2 after the recycled tests (Fig. 8a and b), it can be found that almost all Pt nanoparticles are loaded on the surface of fish-scale flakes, especially on their edges. When the amount of photodeposited Pt is added up to 10 wt%, much more Pt nanoparticles are mainly decorated on the edges of fish-scale flakes (Fig. 9a and b) rather than randomly distributed on the whole surface of FSGNs2, strongly confirming that the novel opened-up fish-scale structured g-C<sub>3</sub>N<sub>4</sub> nanosheet owns unusual

spatial electron transfer property, which makes the photogenerated electrons to preferably transfer along the flat-direction to the edges of fish-scale flakes regardless of the deposited-Pt amount. Fig. 9c and d shows that all Pt nanoparticles with a size of about 4 nm are deposited on the edges of an individual fish-scale flake, further demonstrating the structure-induced special electron transfer path of FSGNs. Additionally, as evidenced by the EDX image of 10 wt% Pt-deposited sample (Fig. 9e), which again manifesting the presence of Pt nanoparticles on the edges of opened-up fish-scale structured nanosheet. Fig. 9f depicts the process of unusual spatial electron transfer of the opened-up fish-scale structured g-C<sub>3</sub>N<sub>4</sub> nanosheet. The edges of opened-up fish-scale flakes are much thinner than their interior flat regions, thus the photogenerated electrons tend to selectively move and gather on the edges fish-scale flakes, similarly to the working principle of the lightning rods [6], ultimately resulting in a highly photogenerated charges separation and transfer efficiency.

Based on the above results, it is well concluded that the origin of outstanding photocatalytic activity of unique opened-up fish-scale structured g-C<sub>3</sub>N<sub>4</sub> nanosheet is confidently derived from its inimitable structure-induced properties. Firstly, the opened-up fish-scale structure is in favor of the visible-light absorption. As mentioned in the DRS analysis in Fig. 4b and c, the FSGNs has multiple scattering and reflecting effects due to spatial distribu-

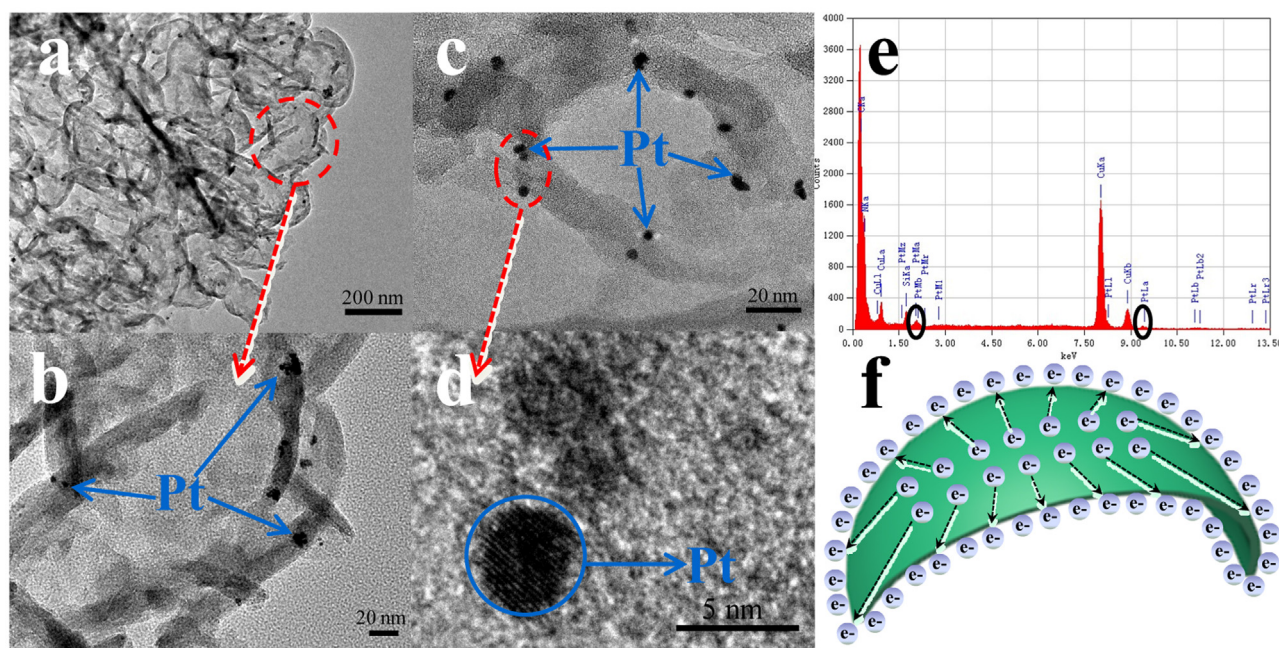


**Fig. 9.** TEM image of (a) 10 wt% Pt-deposited FSGNs2 after 2 h photoreaction. The magnification (b, c) and high-resolution (d) TEM images of 10 wt% Pt-deposited FSGNs2 after 2 h photoreaction. EDX image (e) of 10 wt% Pt-deposited FSGNs2 after 2 h photoreaction. Schematic illustration (f) of unusual spatial electron transfer on the flat of fish-scale flake in the photoreaction process.

tion of the fish-scale flakes, this greatly facilitates photon capture and visible-light absorption. Furthermore, as shown in the analysis including SEM, TEM, nitrogen adsorption-desorption isotherms and pore-size distributions, massive pores (including micropores, mesopores and macropores) as well as exposed edge surfaces of fish scale flakes have been created accompanying the formation of fish-scale structure, which induces abundant defect sites acting as the optical absorption active sites to promote the sunlight harvest. Therefore, it can be deduced that the unique fish-scale microstructure is favorable for the enhancement of visible-light absorption. However, whether or not the improved visible-light absorption is the main factor for the superior photocatalytic activity of the as-prepared samples? This point could find the answer by comparing the basis data of the FSGNs1 and FSGNs3 samples. As above mentioned, FSGNs1 and FSGNs3 have the similar surface area and porosity ( $132.39 \text{ m}^2 \text{ g}^{-1}$  and  $0.6613 \text{ cm}^3 \text{ g}^{-1}$  for FSGNs1,  $130.29 \text{ m}^2 \text{ g}^{-1}$  and  $0.5565 \text{ cm}^3 \text{ g}^{-1}$  for FSGNs3). The two samples also show close PL and transient photocurrent response intensity (Fig. 6), indicating a similar charge separation and transfer capacity. More importantly, it can be found that FSGNs1 exhibits much stronger visible-light absorption compared with FSGNs3 (see DRS results in Fig. 4b), which means that FSGNs1 should show much higher photoactivity relative to FSGNs3. However, FSGNs1 ( $693.09 \mu\text{mol h}^{-1} \text{ g}^{-1}$ ) only displays a slightly higher photocatalytic activity than FSGNs3 ( $645.11 \mu\text{mol h}^{-1} \text{ g}^{-1}$ ). The result strongly revealed that the much stronger optical absorption ability is not main factor in the improvement of HER in the opened-up fish-scale structured  $\text{g-C}_3\text{N}_4$  system.

As the above mentioned, numerous pores (including micropores, mesopores and macropores) and large exposed edge surfaces of fish scale flakes are produced in the well-defined and intact fish-scale structure, thus resulting in a higher active surface area and porosity, especially for FSGNs2 sample ( $210.33 \text{ m}^2 \text{ g}^{-1}$  and  $1.2951 \text{ cm}^3 \text{ g}^{-1}$ , see Table 2). At the front of this discussion, we have eliminated the stronger optical absorption is the main factor to enhance the HER activity, naturally, the edge areas of fish-scale flakes may be the critical factor in photocatalytic hydrogen

evolution due to its unusual spatial electron transfer property. The Pt-deposited experiments have confirmed that the generated edge areas of fish-scale flakes as the real active reaction areas could effectively capture the photogenerated electrons, rather than other expanded areas in the total increased areas. Certainly, when it comes to photogenerated charge separation and transfer, the unusual spatial electron transfer property is well deserved to be discussed. As Fig. 9f depicted, the unique opened-up fish-scale structure promotes the photogenerated electrons to prefer to transfer along the fish-scale flat direction, then arrive at the edge areas of fish-scale flakes, this behavior facilitates the photogenerated electron collection on the edge areas and thus greatly accelerates charges separation and transfer, eventually significantly improves the photocatalytic activity. The above results could be well confirmed by the FSGNs2 basis data: The well-defined and uniform fish-scale structured  $\text{g-C}_3\text{N}_4$  nanosheet (FSGNs2) displays an extremely low PL intensity and a fairly high transient photocurrent response intensity than all other samples (Fig. 6), which is thus leading to a remarkable HER of  $1316.35 \mu\text{mol h}^{-1} \text{ g}^{-1}$ , far outperforming that of others. In summary, the outstanding photocatalytic activity of FSGNs could be primarily attributed to large edge areas of fish-scale flakes and highly-efficient charge separation and transfer, and the two fascinating characteristics are induced by the unusual spatial electron transfer property of  $\text{g-C}_3\text{N}_4$  nanosheet with unique fish-scale structure.

On the basis of the aforementioned results and discussion, a proposed reaction mechanism for visible-light-driven hydrogen evolution is proposed. As shown in Fig. 10, the FSGNs could yield many photogenerated electron-hole pairs under the visible-light illumination. These electrons are rapidly injected into the conduction band (CB) of FSGNs, while the remained holes are consumed by the sacrificial electron donor of TEOA. Then the electrons on the CB transfer to the surface of fish-scale flakes. Because of the above-mentioned unusual spatial electron transfer property of opened-up fish-scale flakes, the electrons migrate along the flat direction to the edges of fish-scale flakes, which remarkably enhanced the separation of photogenerated charges. Then the electrons would gather



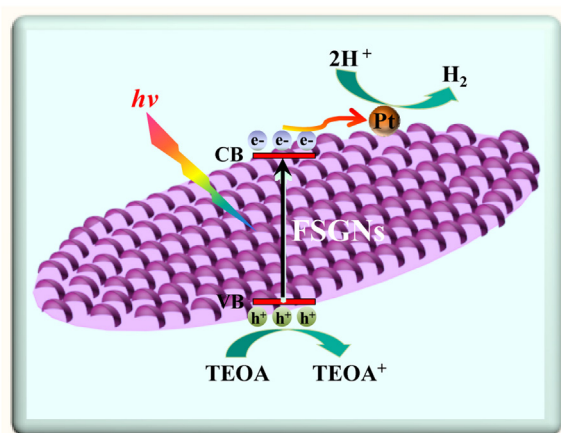


**Fig. 10.** Proposed mechanism of photocatalytic hydrogen evolution for FSGNs2 under visible light irradiation ( $\lambda \geq 420$  nm).

on the surface of Pt nanoparticles that photodeposited on the edges of FSGNs, and interact with the hydrogen ions to generate hydrogen [43–45].

#### 4. Conclusions

In summary, we have successfully constructed a novel opened-up fish-scale structured g-C<sub>3</sub>N<sub>4</sub> nanosheet via a simple one-step solvothermal method. The unique fish-scale structure endows g-C<sub>3</sub>N<sub>4</sub> nanosheet with the unusual spatial electron migration property, which means that the photogenerated electrons selectively migrate along the flat direction to the edges of fish-scale flakes, this reveals the origin of high charge separation efficiency in photocatalytic hydrogen evolution process, and thus contributes to an outstanding photocatalytic activity in hydrogen generation (a HER of 1316.35  $\mu\text{mol h}^{-1} \text{g}^{-1}$ ), nearly 20 and 2.93 times higher than that of bulk g-C<sub>3</sub>N<sub>4</sub> and exfoliated g-C<sub>3</sub>N<sub>4</sub> nanosheet. The research results provide a new insight for the design and synthesis of high-performance photocatalysts with highly-efficient charge separation.

#### Acknowledgements

This work was financially supported by the National Natural Science Foundation of China (Grant No. 21303130), the Fundamental Research Funds for the Central Universities and State Key Laboratory of Heavy Oil Processing (Grant No. SKLOP201602001). Thanks for the technical help from International Center for Dielectric Research (ICDR), Xi'an Jiaotong University, Xi'an, China. The authors also appreciate Mr. Ma and Ms. Dai for their help of using TEM, SEM and EDX, respectively.

#### References

- [1] Y. Zheng, L.H. Lin, X.J. Ye, F.S. Guo, X.C. Wang, *Angew. Chem. Int. Ed.* 53 (2014) 11926–11930.
- [2] W.Z. Wang, J. Xu, *ACS Appl. Mater. Interfaces* 7 (2015) 415–421.

- [3] J. Zhu, K.Y.S. Ng, D. Deng, *ACS Appl. Mater. Interfaces* 6 (2014) 2996–3001.
- [4] B. Lin, G.D. Yang, B.L. Yang, Y.X. Zhao, *Appl. Catal. B: Environ.* 198 (2016) 276–285.
- [5] W.H. Wang, J.Y. Dong, X.Z. Ye, Y. Li, Y.R. Ma, L.M. Qi, *Small* 12 (2016) 1469–1478.
- [6] J.S. Zhang, M.W. Zhang, C. Yang, X.C. Wang, *Adv. Mater.* 26 (2014) 4121–4126.
- [7] R. Kuriki, K. Sekizawa, O. Ishitani, K. Maeda, *Angew. Chem. Int. Ed.* 54 (2015) 2406–2409.
- [8] J. Liang, Y. Zheng, J. Chen, J. Liu, D.H. Jurcakova, M. Jaroniec, S.Z. Qiao, *Angew. Chem. Int. Ed.* 51 (2012) 3892–3896.
- [9] Y. Wang, X.C. Wang, M. Antonietti, *Angew. Chem. Int. Ed.* 51 (2012) 68–89.
- [10] D.J. Martin, K.P. Qiu, S.A. Shevlin, A.D. Handoko, X.W. Chen, Z.X. Guo, J.W. Tang, *Angew. Chem. Int. Ed.* 53 (2014) 9240–9245.
- [11] Y. Zheng, L.H. Lin, B. Wang, X.C. Wang, *Angew. Chem. Int. Ed.* 54 (2015) 12868–12884.
- [12] Y.D. Hou, A.B. Laursen, J.S. Zhang, G.G. Zhang, Y.S. Zhu, X.C. Wang, S. Dahl, I. Chorkendorff, *Angew. Chem. Int. Ed.* 52 (2013) 3621–3625.
- [13] P. Niu, L.L. Zhang, G. Liu, H.M. Cheng, *Adv. Funct. Mater.* 22 (2012) 4763–4770.
- [14] C.B. Liu, L.L. Wang, Y.H. Tang, S.L. Luo, Y.T. Liu, S.Q. Zhang, Y.X. Zeng, Y.Z. Xu, *Appl. Catal. B: Environ.* 164 (2015) 1–9.
- [15] W. Li, D.Y. Zhao, *Adv. Mater.* 25 (2013) 142–149.
- [16] N. Pramanik, T. Imae, *Langmuir* 28 (2012) 14018–14027.
- [17] Q. Han, B. Wang, J. Gao, Z.H. Cheng, Y. Zhao, Z.P. Zhang, L.T. Qu, *ACS Nano* 10 (2016) 2745–2751.
- [18] Y.D. Zou, X.X. Wang, Y.J. Ai, Y.H. Liu, Y.F. Ji, H.Q. Wang, T. Hayat, A. Alsaedi, W.P. Hu, X.K. Wang, *J. Mater. Chem. A* 4 (2016) 14170–14179.
- [19] Y.J. Cui, G.G. Zhang, Z.Z. Lin, X.C. Wang, *Appl. Catal. B: Environ.* 181 (2016) 413–419.
- [20] L. Shi, L. Liang, J. Ma, F.X. Wang, J.M. Sun, *Dalton Trans.* 43 (2014) 7236–7244.
- [21] S.K. Le, T.S. Jiang, Y.W. Li, Q. Zhao, Y.Y. Li, W.B. Fang, M. Gong, *Appl. Catal. B: Environ.* 200 (2017) 601–610.
- [22] J.H. Sun, J.S. Zhang, M.W. Zhang, M. Antonietti, X.Z. Fu, X.C. Wang, *Nat. Commun.* (2012) 1139.
- [23] H. Xu, J. Yan, X.J. She, L. Xu, J.X. Xia, Y.G. Xu, Y.H. Song, L.Y. Huang, H.M. Li, *Nanoscale* 6 (2014) 1406–1415.
- [24] M. Groenewolt, M. Antonietti, *Adv. Mater.* 17 (2005) 1789–1792.
- [25] C. Han, Y.D. Wang, Y.P. Lei, B. Wang, N. Wu, Q. Shi, Q. Li, *Nano Res.* 8 (2015) 1199–1209.
- [26] M.J.M. Batista, O.F. Carceller, A. Kubacka, M.F. García, *Appl. Catal. B: Environ.* 203 (2017) 663–672.
- [27] D.D. Zheng, C.J. Huang, X.C. Wang, *Nanoscale* 7 (2015) 465–470.
- [28] J. Xu, F. Wu, Q. Jiang, Y.X. Li, *Catal. Sci. Technol.* 5 (2015) 447–454.
- [29] W. Chen, T.Y. Liu, T. Huang, X.H. Liu, X.J. Yang, *Nanoscale* 8 (2016) 3711–3719.
- [30] J.J. Niu, J.N. Wang, Y. Jiang, L.F. Su, J. Ma, *Micropor. Mesopor. Mater.* 100 (2007) 1–5.
- [31] B.H. Kim, K.S. Yang, J.P. Ferraris, *Electrochim. Acta* 75 (2012) 325–331.
- [32] D.D. Zheng, G.G. Zhang, X.C. Wang, *Appl. Catal. B: Environ.* 179 (2015) 479–488.
- [33] G.G. Zhang, S.H. Zang, L.H. Lin, Z.A. Lan, G.S. Li, X.C. Wang, *ACS Appl. Mater. Interfaces* 8 (2016) 2287–2296.
- [34] O.F. Carceller, M.J.M. Batista, M.F. García, A. Kubacka, *ACS Appl. Mater. Interfaces* 8 (2016) 2617–2627.
- [35] L.Q. Ye, D. Wu, K.H. Chu, B. Wang, H.Q. Xie, H.Y. Yip, P.K. Wong, *Chem. Eng. J.* 304 (2016) 376–383.
- [36] F. He, G. Chen, Y.S. Zhou, Y.G. Yu, L.Q. Li, S. Hao, B. Liu, *J. Mater. Chem. A* 4 (2016) 3822–3827.
- [37] G.G. Zhang, M.W. Zhang, X.X. Ye, X.Q. Qiu, S. Lin, X.C. Wang, *Adv. Mater.* 26 (2014) 805–809.
- [38] P.K. Chuang, K.H. Wu, T.F. Yeh, H. Teng, *ACS Sustain. Chem. Eng.* 4 (2016) 5989–5997.
- [39] P.W. Chen, K. Li, Y.X. Yu, W.D. Zhang, *Appl. Surf. Sci.* 392 (2017) 608–615.
- [40] X.B. Wei, C.L. Shao, X.H. Li, N. Lu, K.X. Wang, Z.Y. Zhang, Y.C. Liu, *Nanoscale* 8 (2016) 11034–11043.
- [41] K. Takanabe, K. Kamata, X.C. Wang, M. Antonietti, J. Kubota, K. Domen, *Phys. Chem. Chem. Phys.* 12 (2010) 13020–13025.
- [42] S. Chen, C. Wang, B.R. Bunes, Y.X. Li, C.Y. Wang, L. Zang, *Appl. Catal. A: Gen.* 498 (2015) 63–68.
- [43] X.H. Zhang, T.Y. Peng, S.S. Song, *J. Mater. Chem. A* 4 (2016) 2365–2402.
- [44] Y.G. Li, X.B. Cheng, X.Y. Ruan, H. Song, Z.R. Lou, Z.Z. Ye, L.P. Zhu, *Nano Energy* 12 (2015) 775–784.
- [45] S. Martha, A. Nashim, K.M. Parida, *J. Mater. Chem. A* 1 (2013) 7816–7824.